Exploration of Highly Porous Biochar Derived from Dead Leaves to Immobilize LiOH·H₂O Nanoparticles for Efficient Thermochemical Heat Storage Applications

Jichuan Zhang, Yuyuan Zhang,* Hongyu Huang, Kanzai Huang, Lisheng Deng, Huawen Hu,* Menglei Chang, Dongchu Chen, and Yazhuo Wang

The inadequate utilization of low-grade energy from industrial waste heat and solar energy calls for an efficient thermochemical heat storage material. The fabrication of a low-cost but highly efficient composite comprising highly porous biochar and LiOH·H₂O nanoparticles for heat storage applications is reported. The biochar is prepared by the KOH-assisted pyrolysis of dead banyan leaves, and its microstructure and surface properties can be finely tuned by varying the KOH-to-biomass ratio. Such biochar can be mediated to possess a large specific surface area and total pore volume reaching as high as $1255.03 \, m^2 \, g^{-1}$ and $3.65 \, cm^3 \, g^{-1}$, respectively, superior to most previously reported biochar/biocarbon derived from different kinds of waste biomass. Besides, adequate functional groups and a hierarchical porous structure consisting of micropores and mesopores are demonstrated in the prepared biochar. The subsequent hydrothermal reaction with a short duration yields a biochar-LiOH·H₂O composite, where LiOH·H₂O can be homogeneously immobilized with a nanoscale size within the porous biochar matrix. Thus, an enormous biochar/LiOH·H₂O nanoparticles interface can be obtained, resulting in fast hydration reactions with water molecules. Consequently, a significant heat storage density of as high as $3089.6 \, kJ \, kg^{-1}$ is achieved within only 10 min, outstripping some recently reported thermochemical heat storage systems.

1. Introduction

The excessive demand for the fossil fuels, such as coal, natural gases, and petroleum oils, poses a severe threat to the environment due to the accompanied generation of greenhouse gases in large quantities.[1] Therefore, exploring alternative clean and sustainable energy to fossil fuels is highly demanded, where wind, solar, nuclear, and geothermal energies have captured widespread attention. However, the instability of wind energy, the unsafety issue of nuclear energy, and the low utilization efficiency of thermal energy make it necessary to develop a new energy storage system.[2]

Heat storage technologies have received much attention due to their simple operation, low cost, and high heat storage density that can be achieved, rendering their widespread architectural and industrial applications (e.g., special heat supply, water heat supply, and solar energy storage systems).[3,4] More significantly, such technologies' wide distribution and ample energy storage characteristics can impart the ability to harvest low-grade energy (e.g., solar energy and industrial waste heat). However, the instability and the mismatch between energy demand and supply of low-grade energy make it challenging for its utilization.[5] The inefficient use of substantial waste heat produced by industrial manufacturing processes not only wastes valuable energy sources but also even aggravates environmental pollution. Therefore, exploring a highly efficient heat storage technology based on functional materials is highly demanded.

Heat storage technologies can be primarily divided into three basic types based on sensible,[6] latent,[7] and thermochemical[8] heat storage systems. The thermochemical heat storage system has received the most attention attributed to its low energy consumption, high heat storage density, and favorable energy transport among different regions.[9,10] It can also integrate with the concentrated solar energy system for low-grade energy harvesting. Metal hydroxides, metal hydrides, metal carbonates, and inorganic hydrates are the most promising functional materials for constructing thermochemical heat storage systems.[4,10,11]

J. Zhang, Y. Zhang, K. Huang, H. Hu, M. Chang, D. Chen
School of Materials Science and Hydrogen Energy
Foshan University
Foshan, Guangdong 528000, China
E-mail: zhangyuyuan@fosu.edu.cn; huawenhu@fosu.edu.cn

Y. Zhang, H. Hu, M. Chang, D. Chen
Guangdong Key Laboratory for Hydrogen Energy Technologies
Foshan, Guangdong 528000, China

H. Huang, L. Deng
Guangzhou Institute of Energy Conversion
Chinese Academy of Sciences
Wushan, Guangzhou 510640, China

Y. Wang
Qingyuan Kebo Environmental Protection Technology Co., Ltd.
No. 18, Chuangxing Avenue, High-Tech Industrial Development Zone,
Qingyuan, Guangdong 511500, China

ADVANCED
SCIENCE NEWS
www.advancedsciencenews.com

Energy Technology
Generation, Conversion, Storage, Distribution
www.entechnol.de

The inorganic lithium hydroxide monohydrate ($LiOH \cdot H_2O$) has been extensively applied in the thermochemical heat storage system due to its high energy storage density (1440 kJ kg^{-1}) and low reaction temperatures (e.g., $\approx$340 K[12]). Therefore, such a material can be effectively applied to store waste heat generated by low-grade thermal energy sources such as industrial waste heat and solar heat collecting devices. However, the low hydration rate of $LiOH \cdot H_2O$ causes unsatisfactory efficiency in heat storage, and the hydration of $LiOH \cdot H_2O$ at 303 K and 80% relative humidity for 60 min only results in a hydration ratio of as low as 0.24. Moreover, the heat release rate is usually low during the exothermic process.[12]

In these contexts, the exploration of novel thermochemical heat storage material based on $LiOH \cdot H_2O$ is thus imperative to improve the heat storage and utilization efficiency. Many kinds of substrates (e.g., 3D carbon, graphene, carbon nanotubes, and hydrophilic substances[5,13,14]) have been employed to combine with $LiOH \cdot H_2O$ to form various composites, where the size and morphology of $LiOH \cdot H_2O$ can be varied by tuning the type, structure, and surface properties of substrates. Although combining the substrates with $LiOH \cdot H_2O$ increases the heat storage density to a certain extent, the high cost of these carbonaceous substrates and still unsatisfactory heat storage density achieved using some hydrophilic substrates restrain the large-scale applications of the composites with $LiOH \cdot H_2O$.

We demonstrate a low-cost but efficient waste biomass-derived biochar substrate to immobilize $LiOH \cdot H_2O$, a promising alternative to the expensive carbon nanomaterials and inefficient hydrophilic substrates. Such a material design can address the environmental contamination and value-added natural resource wasting issues because the incineration commonly employed to process waste biomass generate hazardous/toxic gaseous species and solid wastes can be avoided.[15] More importantly, this biochar possesses the ability to finely tune the size and morphology of $LiOH \cdot H_2O$ particles, rendering homogeneous immobilization of $LiOH \cdot H_2O$ with a nanoscale size.

Due to its high efficiency, straightforward operation, and low cost, one-step carbonization is adopted for the present biochar synthesis, which might be superior to many previously reported two-step methods and template-assisted approaches.[16] This study systematically investigates the effects of the KOH-to-biomass ratio on the biochar structure and surface properties in a one-step straightforward carbonization process. Meanwhile, the impact of the loading content of $LiOH \cdot H_2O$ on the structure of the biochar-based composites is clarified. The mechanism underlying the promotion effect of the biochar substrate is also unraveled. The main content of the present study is schematically illustrated in **Figure 1**.

2. Results and Discussion

2.1. X-Ray Diffraction Analysis

Figure 2 shows the X-Ray diffraction (XRD) patterns of various prepared samples. The diffraction bands at $\approx$21.18°, 30.44°, 31.65°, 34.01°, 36.03°, 36.85°, 43.43°, 48.73°, 56.67°, and 61.33° can be assigned to the characteristic diffraction planes of $LiOH \cdot H_2O$.[5,13,17] An increase in the content of $LiOH \cdot H_2O$ within the composite leads to an enhancement of these diffraction bands when progressing from 20%K-BC3/$LiOH \cdot H_2O$, 40%K-BC3/$LiOH \cdot H_2O$, 60%K-BC3/$LiOH \cdot H_2O$, to 80%K-BC3/$LiOH \cdot H_2O$. The diffraction peak at $\approx$23.25° and 39.76° can be indexed to the graphitic (002) and (100) planes, thus implying the existence of biochar compositions.[18]
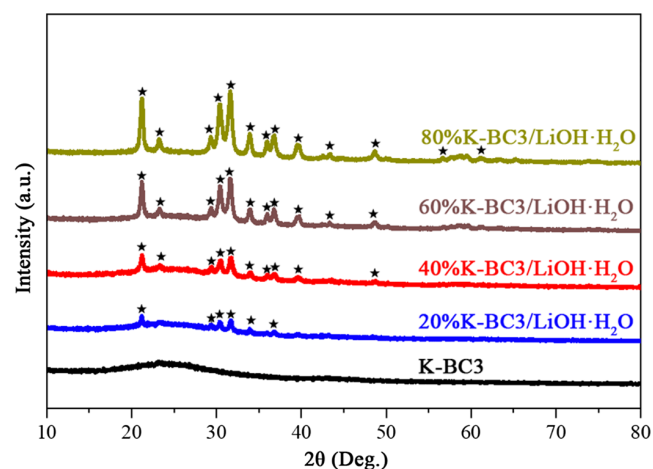

Figure 2. X-Ray diffraction (XRD) patterns of the $LiOH \cdot H_2O$, 20%K-BC3/$LiOH \cdot H_2O$, 40%K-BC3/$LiOH \cdot H_2O$, 60%K-BC3/$LiOH \cdot H_2O$, and 80%K-BC3/$LiOH \cdot H_2O$ samples.
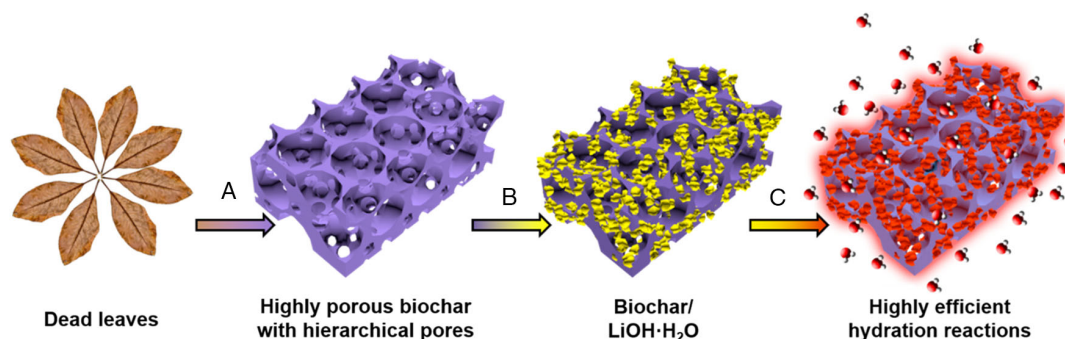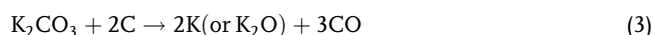

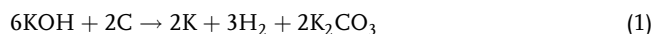**Figure 1.** Schematic illustration of the main content of the present study, primarily including: a) waste biomass conversion to produce a highly porous biochar material, b) controllable immobilization of $LiOH \cdot H_2O$ nanoparticles onto the porous biochar substrate, and c) investigation of the hydration efficiency of the biochar-immobilized $LiOH \cdot H_2O$ for superior thermochemical heat storage applications.

The broad and diffused diffraction peaks indicate the excellent dispersion of LiOH·H$_2$O in an ultrasmall size within the biochar matrix.

2.2. Observation of the Porous Structure of the Prepared Biochar by Scanning Electron Microscope

The surface morphology evolution of the biochar subject to KOH activation can be reflected by scanning electron microscope (SEM) images, as shown in **Figure 3**a–d. The KOH-assisted calcination of banyan biomass can produce porous biochar materials enriched with abundant surface functionalities. Several key reactions have been proposed for the KOH-assisted biomass conversion process based on Equation (1)–(4).[19] The etching of the carbon framework and the concomitant release of gases loosen the biochar structure, improve the specific surface area, and generate high porosity.

$$6KOH + 2C \rightarrow 2K + 3H_2 + 2K_2CO_3 \tag{1}$$

$$K_2CO_3 \rightarrow K_2O + CO_2 \tag{2}$$

$$K_2CO_3 + 2C \rightarrow 2K(or\ K_2O) + 3CO \tag{3}$$

$$K_2O + C \rightarrow 2K + CO \tag{4}$$

Although it is not easy to clarify the KOH ratio effect on the microstructure of the K-BC samples from the SEM images, the use of KOH indeed enables the formation of numerous pores across the biochar substrate. We further use TEM, N$_2$ adsorption-desorption measurements, and the Fourier transform infrared (FTIR) spectroscopy and X-ray photoelectron spectroscopy (XPS) to clarify the structure and surface functionalities of the biochar sample mediated by the biomass-to-KOH ratio, as we shall see later.

2.3. Brunauer–Emmett–Teller (BET) Analysis

We further characterize the prepared biochar samples' surface area and porous structure (including p-BC, K-BC1, K-BC2, and K-BC3) by the BET method, with the results summarized in **Figure 4**, **Table 1**, and Figure S1 and S2, Supporting Information. The KOH-assisted calcination significantly improves the specific surface area, total pore volume, and average pore diameter (Table 1). The sharp increases in the low relative pressure region shown in Figure 6 imply the presence of micropores in the structure of these samples, while the distinct hysteresis loop in the middle to high relative pressure range reveals that mesopores exist in the structure of the K-BC3 sample as well.[20]

Such a hierarchical porous structure can help disperse and stabilize LiOH·H$_2$O nanoparticles. K-BC3 exhibits an enormous specific surface area and total pore volume reaching as high as 1255.03 m^2 g^{-1} and 3.65 cm^3 g^{-1}, respectively, which are larger than K-BC1 and K-BC2 samples (Table 1, Figure S1 and S2, Supporting Information) and considerably greater than the p-BC sample and our previously reported pomelo peels-derived porous biochar,[21] corncob biomass-derived porous biochar,[15] and municipal sludge-derived hierarchical biocarbon,[22] as well as other biochar most recently reported elsewhere.[23] This finding also reveals that KOH plays a pivotal role in constructing highly porous biochar with a large specific surface area. Such a large surface area and pore volume reveal that the banyan-leaves-derived K-BC3 can provide sufficient active surface for dispersing a large amount of LiOH·H$_2$O at the nanoscale.

2.4. Surface Functionality Characterization by FTIR and XPS

To further unveil the surface functionalities of various samples, we provide their FTIR spectra and XPS results in **Figure 5**, **Table 2**, and Figure S3, Supporting Information. Although one cannot find an apparent difference in the FTIR spectra of the p-BC and K-BC samples, their surface functional groups can be revealed. The FTIR absorption band at 3600 cm^{-1} is due to the stretching vibrations of -OH in phenol groups and water molecules.[24] The absorption band at 1450 cm^{-1} can be ascribed to the bending vibration of -OH groups.[25] The -C=C- group of benzene rings can be evidenced by the emergence of the absorption bands in the range of 1510–1600 cm^{-1}.[26] The absorption bands at 2850 and 1350 cm^{-1} can correspond to the -CH group of alkane moieties.[27] The absorption peak at 760 cm^{-1} in the fingerprint range can be indexed to aromatic groups.[19] Thus, numerous functional groups are confirmed in the backbone of the K-BC samples, thus providing a hydrophilic interface for hydration reactions between LiOH·H$_2$O and water molecules. XPS spectra are further provided to reveal the difference in the atomic percentage of the carbon and surface heteroatoms for the prepared biochar samples mediated by the biomass-to-KOH ratio (Table 2 and Figure S3, Supporting Information). The larger addition amount of KOH can lead to a higher heteroatom (oxygen and nitrogen) percentage, especially oxygen, due to the prominent reaction activity of KOH that highly corrosively etches the internal structure of the biochar to generate high porosity (Table 1) and adequate surface functionalities (Figure 5 and Table 2).

The oxygen and nitrogen-containing functional groups can also stably anchor LiOH·H$_2$O particles, facilitating the formation of a durable thermochemical heat storage system. Notably, after
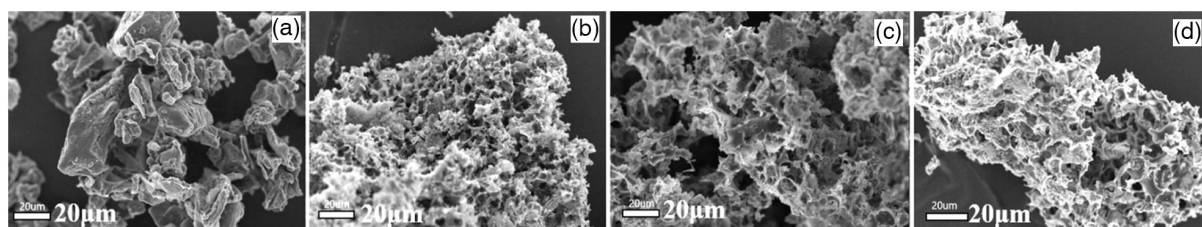

Figure 3. SEM images of: a) the p-BC, b) K-BC1, c) K-BC2, and d) K-BC3 samples.
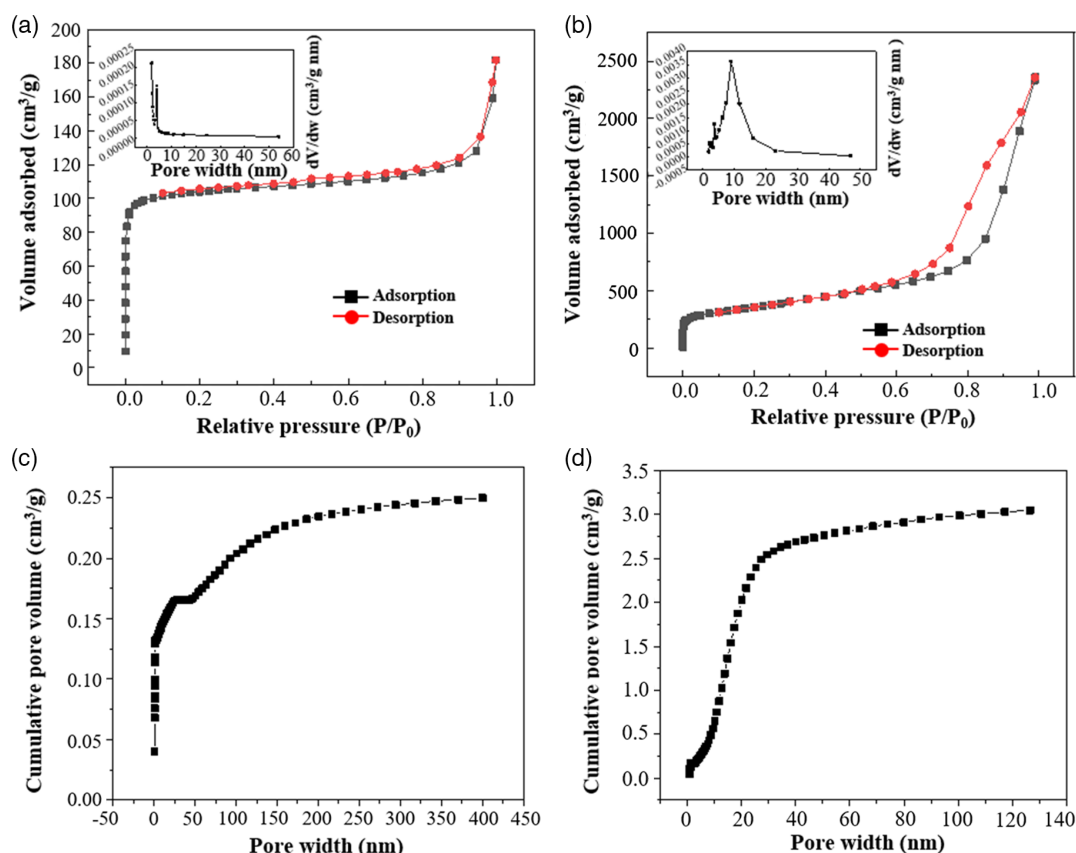
Figure 4. N_2 adsorption–desorption isotherms for the a) p-BC and b) K-BC3 samples. Plots of pore size versus cumulative pore volume for the c) p-BC and d) K-BC3 samples. Insets in (a,b) correspond to the pore size distribution plots.

Table 1. Specific surface area and pore analysis of the prepared p-BC, K-BC1, K-BC2, and K-BC3 samples.

Samples	BET specific surface area [$m^2\,g^{-1}$]	Total pore volume [$cm^3\,g^{-1}$]	Pore size on average [nm]
p-BC	354.63	0.25	9.29
K-BC1	1018.48	0.57	7.16
K-BC2	1041.95	0.51	5.39
K-BC3	1255.03	3.65	10.65

the LiOH·H_2O deposition onto the K-BC surface, the FTIR absorption intensities become weakened to some extent (Figure 5), which probably results from the interfacial interactions between the surface functional groups of K-BC and LiOH·H_2O.

2.5. Morphology Analysis of the K-BC/LiOH·H_2O Composites by SEM

Figure 6 shows the SEM images of various K-BC/LiOH·H_2O composites with different loading contents of LiOH·H_2O, revealing that the increase of LiOH·H_2O loading onto K-BC3 substrate aggravates the aggregation extent of LiOH·H_2O. It can also be
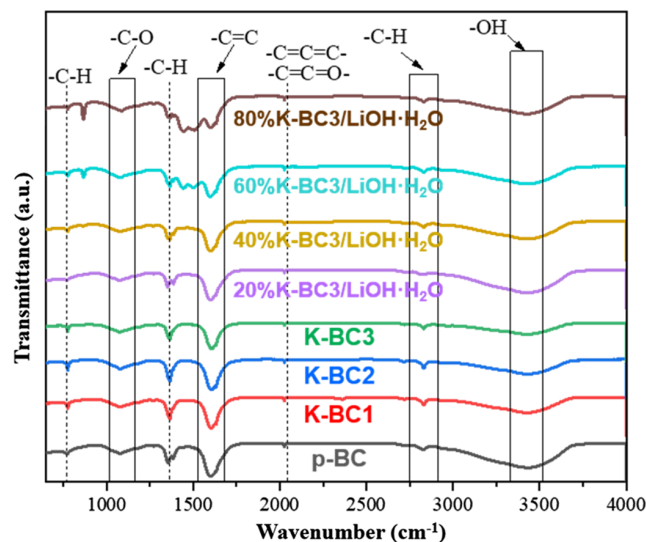

Figure 5. FTIR spectra of p-BC, K-BC1, K-BC2, K-BC3, 20%K-BC3/LiOH·H_2O, 40%K-BC3/LiOH·H_2O, 60%K-BC3/LiOH·H_2O, and 80%K-BC3/LiOH·H_2O.

noted that the appropriate content of LiOH·H_2O facilitates the formation of well-dispersed particles within the porous K-BC matrix. The overloading of LiOH·H_2O (in this case,

**ADVANCED
SCIENCE NEWS**

www.advancedsciencenews.com

Energy Technology
Generation, Conversion, Storage, Distribution

www.entechnol.de

Table 2. Atomic percentages of different atoms calculated based on XPS characterizations.

Sample	Biomass-to-KOH weight ratio	C [at%]	N [at%]	O [at%]
p-BC	1:0	83.9	1.23	14.87
K-BC1	1:0.8	78.64	1.14	20.22
K-BC2	1:1	75.66	1.35	22.99
K-BC3	1:1.2	71.57	1.62	26.81

80%K-BC3/LiOH·H_2O) results in the formation of buck sheet-like structure with continuously connected LiOH·H_2O, and the nanoparticle morphology can no longer be observed, stemming from the severe aggregation of LiOH·H_2O at a high loading content.

2.6. Microstructural Observation of Typical Samples by Transmission Electron Microscope

We then employ transmission electron microscope (TEM) to characterize the microstructure of the typical biochar and its composite with LiOH·H_2O (namely, K-BC3 and 20%K-BC3/LiOH·H_2O), with the results presented in **Figure 7**a–d. The TEM images of bare LiOH·H_2O are also provided in Figure S4, Supporting Information, for comparison. The K-BC3 sample exhibits a clean surface without a distinguished secondary crystalline phase. In addition, K-BC3 also presents the microporous structure under TEM with smooth pore walls, and no particles can be noted on the surface (Figure 7a,b). By contrast, after the hydrothermal deposition of LiOH·H_2O, the resulting 20%K-BC3/LiOH·H_2O sample exhibits an entirely different morphology from that of pristine K-BC3 due to the emergence of secondary crystalline phases indexed to LiOH·H_2O (Figure 7c,d). The LiOH·H_2O particles are well dispersed over the K-BC3 surface with intimate interfacial contact, likely due to the strong interactions between porous structure bearing oxygen and nitrogen functionalities and LiOH·H_2O particles. The average particle size of the dispersed LiOH·H_2O particles can

be estimated to be 20–50 nm, notably smaller than that of bare LiOH·H_2O particles without K-BC3 (Figure S4, Supporting Information). It can be noted that the bare LiOH·H_2O particles show a severe aggregation, with a micron size, consisting of many particles with an average size of several hundred nanometers. These results provide direct evidence for presenting the critical role of the K-BC3 substrate in the sufficient dispersion and immobilization of LiOH·H_2O, producing nanoscale particles within the porous and oxygen-rich biochar matrix and thus being favorable for obtaining superior thermochemical heat storage performance.

2.7. Thermogravimetric-Differential Scanning Calorimetry Analysis

It has been reported that pure LiOH·H_2O possesses a heat storage density of as high as 1440 kJ kg^{-1}.[12] Nevertheless, the low hydration rate and poor thermal conductivity limit the thermal storage performance, thus implying that the combination of LiOH·H_2O with biochar might enhance the thermochemical heat storage performance by considering the supplemental and synergistic benefits brought by the biochar. The heat storage density of the composite samples can be estimated based on the thermogravimetric-differential scanning calorimetry (TG-DSC) analysis shown in **Figure 8**a–f. To more clearly distinguish the difference in the heat storage density calculated based on TG-DSC among various samples, including the present samples bearing different compositions and structures and the recently reported LiOH·H_2O-based materials, we also provide a histogram for intuitive comparison, as presented in **Figure 9**.

After 10 min hydration under humid conditions, the 20%K-BC3/LiOH·H_2O sample exhibits the heat storage density of 3089.6 kJ kg^{-1} (Figure 8c), much higher than that for pure LiOH·H_2O with a full hydration state, as well as 20%K-BC1/LiOH·H_2O (1285.4 kJ kg^{-1}, Figure 8a), 20%K-BC2/LiOH·H_2O (1618.5 kJ kg^{-1}, Figure 8b), and other recently reported LiOH·H_2O-based thermochemical heat storage materials (Figure 9).[5,13,17] This finding can be attributed to the presence of highly porous K-BC3 that acts as superior support to disperse LiOH·H_2O, thus increasing the contract surface area
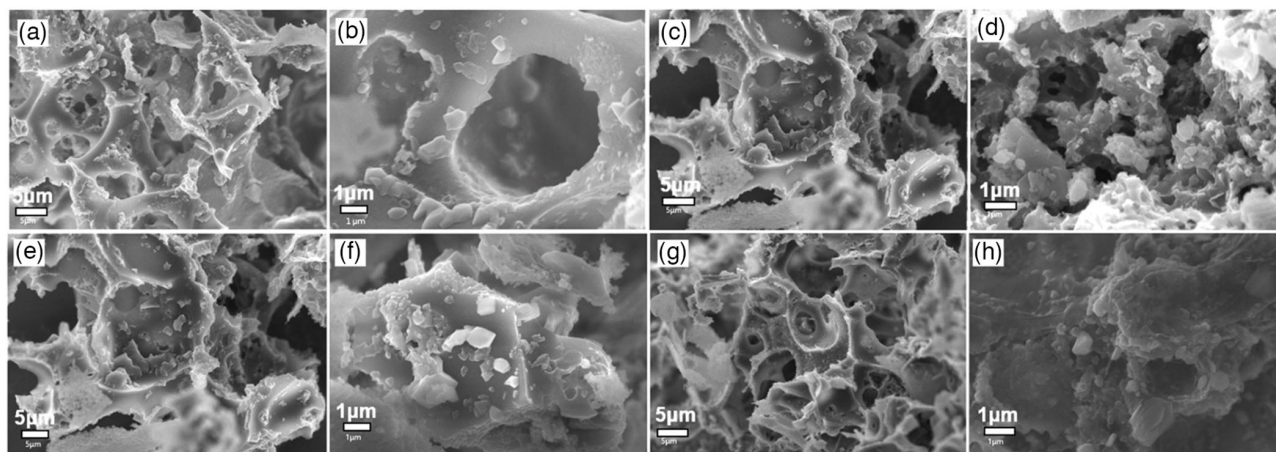

Figure 6. SEM image of the 20%K-BC3/LiOH·H_2O (a,b), 40%K-BC3/LiOH·H_2O (c,d), 60%K-BC3/LiOH·H_2O (e,f), and 80%K-BC3/LiOH·H_2O (g,h) samples. Note that b, d, f, and h are the corresponding SEM images at higher magnification scales relative to a, c, e, and g, respectively.
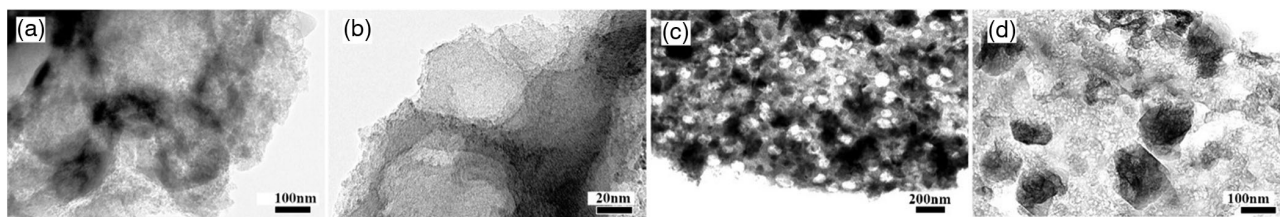
Figure 7. TEM images of a,b) K-BC3 and c,d) 20%K-BC3/LiOH·H$_2$O. Note that (b) and (d) are the corresponding TEM images at higher magnification scales relative to (a) and (c), respectively.
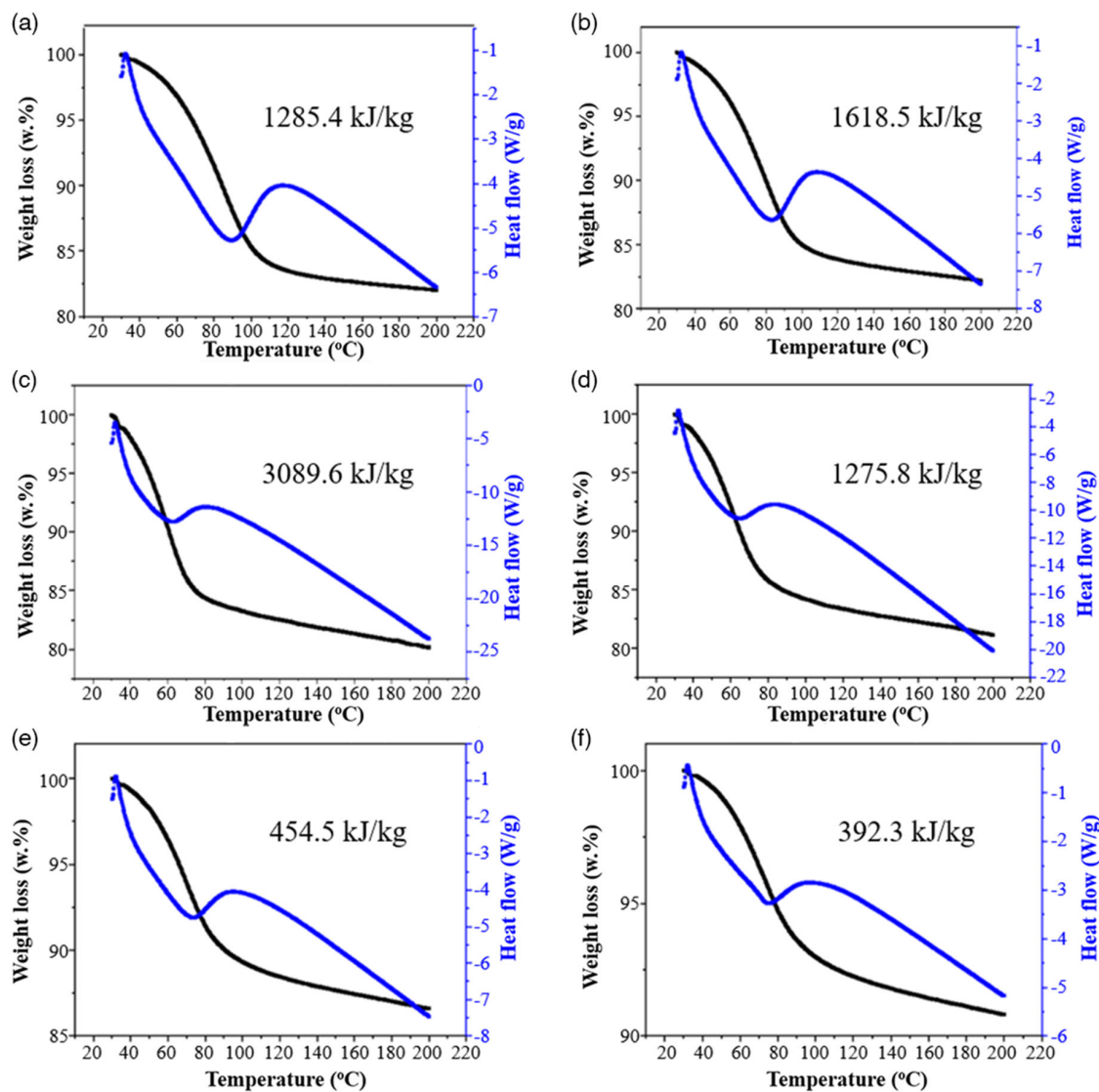

Figure 8. TG-DSC curves of the a) 20%K-BC1/LiOH·H$_2$O, b) 20%K-BC2/LiOH·H$_2$O, c) 20%K-BC3/LiOH·H$_2$O, d) 40%K-BC3/LiOH·H$_2$O, e) 60%K-BC3/LiOH·H$_2$O, and f) 80%K-BC3/LiOH·H$_2$O samples.

between LiOH·H$_2$O and water molecules (Table 1). Besides, K-BC3 also possesses an adsorption capability due to its numerous hydrophilic functional groups that can concentrate water molecules at the K-BC3/LiOH·H$_2$O interface (Figure 5 and Table 2). Consequently, the fast hydration of highly dispersed LiOH·H$_2$O

nanoparticles is realized. More importantly, increasing the KOH-to-biomass ratio leads to the biochar samples capable of elevating heat storage density of its composite with LiOH·H$_2$O, with the following order: 20%K-BC3/LiOH·H$_2$O (3089.6 kJ kg^{-1}) >20% K-BC2/LiOH·H$_2$O (1618. 5 kJ kg^{-1}) >20%K-BC1/LiOH·H$_2$O
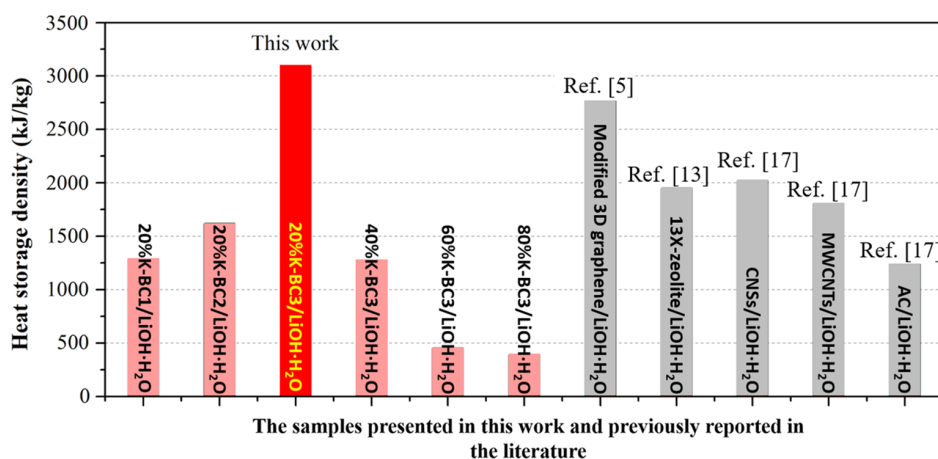
Figure 9. Histogram of comparing heat storage densities of different samples including 20%K-BC1/LiOH·H_2O, 20%K-BC2/LiOH·H_2O, 20%K-BC3/LiOH·H_2O, 40%K-BC3/LiOH·H_2O, 60%K-BC3/LiOH·H_2O, and 80%K-BC3/LiOH·H_2O fabricated in this work, as well as the recently reported LiOH·H_2O-based composite materials (where 3D, CNNs, MWCNTs, and AC are the abbreviations of three-dimensional, carbon nanospheres, multi-walled carbon nanotubes, and activated carbon, respectively).

(1285.4 kJ kg^{-1}), as shown in Figure 8a–c and 9. Thus, KOH-imparted benefits are demonstrated, that is, enlarging surface area and enriching porous structure and surface functionalities since the higher the content of KOH, the more intense the reaction that occurs during the KOH-assisted calcination reactions (Equation (1)–(4)). The highly porous structure with a large surface area and adequate surface groups is favorable for sufficiently dispersing and stabilizing LiOH·H_2O nanoparticles resulting from the space-confining and complexation effects from the abundant pores and surface functional groups, respectively, thus significantly increasing the heat storage density of LiOH·H_2O. Furthermore, the nanosize of the LiOH·H_2O particles immobilized within the highly porous K-BC3 matrix enables the exposure of their numerous unsaturated surface atoms without bonding adjacent atoms. As a result, these existing dangling bonds promote water adsorption and hydration reactions. The nanoscale dispersion of LiOH·H_2O within the K-BC3 matrix is evidenced by SEM and TEM shown in Figure 6 and 7, respectively.

With the fixed biochar substrate to K-BC3, an increase in the loading of LiOH·H_2O debases the heat storage density (**Figure** 8c–f, and **9**). Specifically, progressing from 20%K-BC3/LiOH·H_2O, 40%K-BC3/LiOH·H_2O, 60%K-BC3/LiOH·H_2O, to 80%K-BC3/LiOH·H_2O, one can note that the heat storage density is lowered from 3089.6, 1275.8, 454.5, to 392.3 kJ kg^{-1}, as shown in Figure 8c–f, respectively. Therefore, the LiOH·H_2O loading content should be cautiously selected. This is because a high loading is likely to induce the aggregation of LiOH·H_2O particles (as evidenced by the SEM images presented in **Figure 6**), causing a decrease in the accessible surface area and, consequently, the degradation of the thermochemical heat storage performance.[5,13]

3. Conclusions

We have presented a superior biochar material derived from natural waste biomass (i.e., dead banyan leaves), which is

demonstrated to be a superior substrate in combining with LiOH·H_2O. The biochar microstructure and surface properties can be finely tuned by varying the KOH-to-biomass weight ratio in a straightforward calcination process, and the optimized biochar possesses a huge specific surface area and total pore volume reaching as high as 1255.03 m^2 g^{-1} and 3.65 cm^3 g^{-1}, respectively, which are higher than most of the biochar derived from other kinds of biomasses. Such a large surface area of the prepared biochar provides an enormous biochar/LiOH·H_2O interface for contact with water molecules. In addition, the numerous oxygen and nitrogen-containing functional groups (especially oxygen) on the biochar surface provide superior affinity to water molecules. The nanoscale dispersion of LiOH·H_2O over the biochar surface also exposes a myriad of unsaturated surface atoms with dangling bonds, contributing to high affinity to water molecules. The collective effect promotes the hydration reaction of the optimized biochar-LiOH·H_2O composite, and an impressive heat storage density of as high as 3089.6 kJ kg^{-1} is achieved, outstripping most of the previously reported LiOH·H_2O-based systems. Therefore, the low-cost but highly efficient biochar derived from naturally abundant and renewable waste biomass holds excellent potential for thermal energy harvesting applications and beyond.

4. Experimental Section

Raw Materials: Waste biomass (in this case, banyan leaves) was collected from the campus. KOH and LiOH·H_2O of analytic grades were purchased from Guangdong Guanghua Sci.-Tech. Co., Ltd. and Shanghai Tandan Sci.-Tech. Co., Ltd., respectively. All other chemicals were analytic reagents and used without further purification unless stated otherwise.

Preparation of Highly Porous Biochar by KOH-Assisted Calcination: Highly porous biochar was prepared by the KOH-assisted calcination of biomass powder obtained from dead banyan leaves. Specifically, the biomass powder (6.0 g) was mixed with KOH at different biomass-to-KOH ratios (1:0.8, 1:1, and 1:1.2) by ball milling. The parameters for ball milling, including rotation speed, grinding media-to-material weight ratio, and ball milling time, were set to 400 r min^{-1}, 8:1, and 30 min, respectively. After
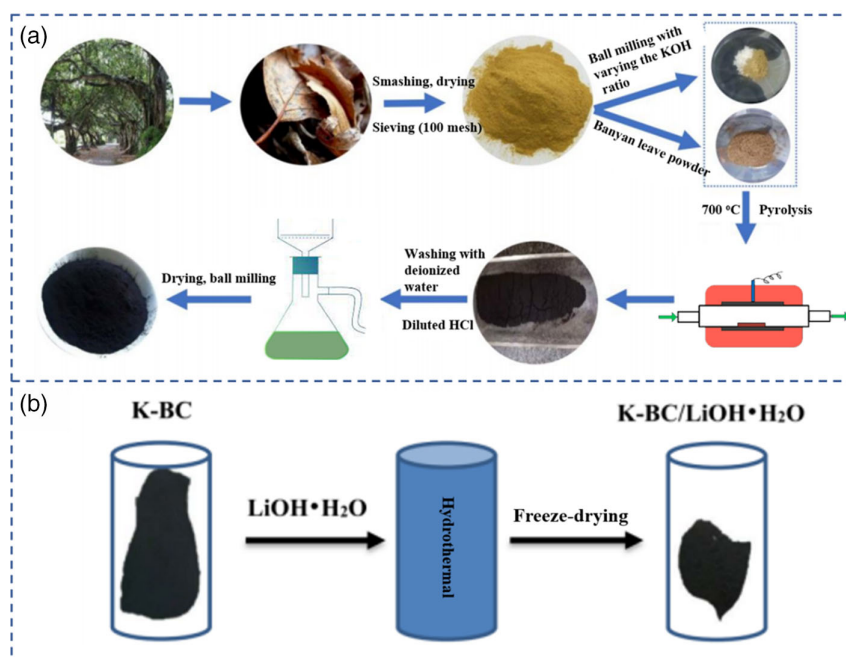
Figure 10. Schematic illustration of the preparation of dead leaves-derived biochar and its composites with LiOH·H_2O by a) KOH-assisted pyrolysis and b) hydrothermal reactions, respectively.

homogenization, the mixture was placed into a tubular furnace pre-flowed with N_2 for 20 min. The calcination conditions were set as follows: the furnace was heated at a rate of 10 °C min^{-1} until reaching 700 °C, and a residential time of 1 h was executed. The selection of such a calcination temperature was based on the previous work, with the results showing that an optimized specific surface area and total pore volume could be obtained at ≈700 °C.[28] After the thermal treatment, the furnace was cooled down before the powder was withdrawn. The collected powder was then cleaned with deionized water and hydrochloric acid until neutral. The procedures for acid washing were provided as follows: the biochar prepared via pyrolysis was put into a beaker at room temperature. Then, a 1 mol L^{-1} hydrochloric acid solution was added until the mixture became acidic. After the acid impregnation had been sustained for 30 min at room temperature, the mixture was filtered under vacuum and washed sufficiently with deionized water until neutral. The washed filter cake was finally dried at 80 °C and stored in a desiccator before use. The samples prepared at the biomass-to-KOH ratios of 1:0.8, 1:1, and 1:1.2 were labeled as K-BC1, K-BC2, and K-BC3, respectively. For comparison, pristine biomass powder was also directly processed with the procedures described above, except KOH was not added, yielding the sample designated as p-BC. We also present a schematic route to illustrate the preparation process, as shown in **Figure 10**a. The biochar yields were also calculated (as shown in Table S1 and Figure S5, Supporting Information). Although the higher KOH amount resulted in a lower yield due to the intensive etching reactions with KOH, the difference among K-BC1, K-BC2, and K-BC3 was not obvious.

Preparation of Biochar-LiOH·H_2O Composites by Hydrothermal Reactions: With the prepared biochar (K-BC1, K-BC2, and K-BC3), a hydrothermal method was adopted to prepare K-BC/LiOH·H_2O composites. The preparation process is schematically illustrated in **Figure 10**b. Briefly, the prepared K-BC, LiOH·H_2O, and deionized water (50 mL) were placed into a polytetrafluoroethylene-lined mold of a hydrothermal reactor and then subjected to ultrasonication at 30 °C for 2 min before the hydrothermal reaction. While fixing the total mass of K-BC and LiOH·H_2O to 300 mg, the weight percentage of LiOH·H_2O was varied from 20%, 40%, 60%, to 80%. The hydrothermal reaction proceeded at 105 °C for 12 h. After the reaction, the mold was taken out to cool down, and the sample

was transferred to a beaker that was subsequently subject to freeze-drying treatment. The freeze-dried sample was placed in a vacuum oven at 150 °C and kept for 2 h. The finally produced samples were designated as 20%K-BC/LiOH·H_2O, 40%K-BC/LiOH·H_2O, 60%K-BC/LiOH·H_2O, and 80%K-BC/LiOH·H_2O, corresponding to the LiOH·H_2O percentages of 20%, 40%, 60%, and 80%, respectively.

For hydration reactions, the prepared composites were placed in a test chamber at a constant temperature of 30 °C and a humidity of 80%, and the hydration reaction time was fixed to 10 min. The TG-DSC measurements were performed to evaluate the thermal storage performance of the prepared samples using a Mettler Toledo thermogravimetric analyzer (TGA/DSC3+).

Characterizations: The morphologies of the prepared samples were characterized using a cold-field emission SEM, S-4800, Hitachi, Co., Ltd. The microstructures of the typical samples were further examined using a high-resolution field-emission TEM, JEOL JEM-2100 F, at a voltage of 200 kV. The phase structure of the samples was inspected using powder XRD equipment (Bruker, Germany), with the Cu Kα radiation operated at 40 kV and 40 mA. A scan step size and count time were set to 0.0167° and 10.160 s, respectively. The N_2 adsorption–desorption test was employed based on the Brunauer–Emmet–Teller (BET) method using a Quantachrome QDS-30 analyzer to obtain the specific surface area and pore size distribution over the relative pressure range of 0.1–1.0.

Supporting Information

Supporting Information is available from the Wiley Online Library or from the author.

Acknowledgements

Conflict of Interest

The authors declare no conflict of interest.

Author Contributions

J.Z.: Investigation, Data curation, and Writing - original draft. Y.Z.: Conceptualization, Methodology, Funding acquisition, Supervision, and Writing - original draft. H.H.: Conceptualization, Formal analysis, Project administration, Funding acquisition, Validation, Methodology, Supervision, Writing - review and editing. H.H., K.H., L.D., and Y.W.: Software, Resource, and Writing - review and editing. M.C., and D.C.: Conceptualization, Data curation, Formal analysis, and Writing - review and editing.

Data Availability Statement

The data that support the findings of this study are available from the corresponding author upon reasonable request.

Keywords

[1] a) D. Aydin, S. P. Casey, S. Riffat, *Renew. Sust. Energy Rev.* **2015**, *41*, 356; b) H. Hu, J. Z. Ou, X. Xu, Y. Lin, Y. Zhang, H. Zhao, D. Chen, M. He, Y. Huang, L. Deng, *Chem. Eng. J.* **2021**, *425*, 130587; c) A. J. Carrillo, J. González-Aguilar, M. Romero, J. M. Coronado, *Chem. Rev.* **2019**, *119*, 4777; d) Y. Zhang, H. Hu, M. Chang, H. Wei, D. Chen, M. Zhang, L. Wu, X. Li, *J. Mater. Sci.* **2017**, *53*, 2102.

[2] a) A. C. M. Griffond, M. V. Sofianos, D. A. Sheppard, T. D. Humphries, A.-L. Sargent, M. Dornheim, K.-F. Aguey-Zinsou, C. E. Buckley, *J. Alloys Compd.* **2021**, *858*, 158229; b) K. E. N'Tsoukpoe, F. Kuznik, *Renew. Sust. Energy Rev.* **2021**, *139*, 110683.

[3] a) H. Kerskes, F. Bertsch, B. Mette, A. Wörner, F. Schaube, *Chem. Ing. Tech.* **2011**, *83*, 2014; b) G. Krese, V. Butala, U. Stritih, *Energy Build.* **2018**, *164*, 239; c) B. Sarrion, J. M. Valverde, A. Perejon, L. Perez-Maqueda, P. E. Sanchez-Jimenez, *Energy Technol.* **2016**, *4*, 1013.

[4] a) L. F. Cabeza, A. Solé, C. Barreneche, *Renew. Energy* **2017**, *110*, 3; b) H. Wei, H. Hu, M. Chang, Y. Zhang, D. Chen, M. Wang, *Ceram. Int.* **2017**, *43*, 12472.

[5] L. Li, S. Li, T. Zeng, L. Deng, H. Huang, J. Li, N. Kobayshi, L. Liu, Y. Zhou, *Energy Technol.* **2021**, *9*, 2001086.

[6] a) H. Niyas, L. Prasad, P. Muthukumar, *Clean Technol. Environ. Policy* **2015**, *17*, 501; b) G. Li, *Renew. Sust. Energy Rev.* **2016**, *53*, 897.

[7] a) Y. Tao, Y.-L. He, *Renew. Sust. Energy Rev.* **2018**, *93*, 245; b) W. Aftab, A. Usman, J. Shi, K. Yuan, M. Qin, R. Zou, *Energy Environ. Sci.* **2021**, *14*, 4268.

[8] Y. Zhao, C. Zhao, C. Markides, H. Wang, W. Li, *Appl. Energy* **2020**, *280*, 115950.

[9] a) H. Jarimi, D. Aydin, Z. Yanan, G. Ozankaya, X. Chen, S. Riffat, *Int. J. Low-Carbon Technol.* **2019**, *14*, 44; b) D. Liu, L. Xin-Feng, L. Bo, Z. Si-Quan, X. Yan, *Int. J. Energy Res.* **2018**, *42*, 4546.

[10] a) A. I. Shkatulov, Y. Aristov, *Energy Technol.* **2018**, *6*, 1844; b) K. Randhir, K. King, J. Petrasch, J. Klausner, *Energy Technol.* **2020**, *8*, 2000063; c) N. C. Preisner, T. Block, M. Linder, H. Leion, *Energy Technol.* **2018**, *6*, 2154; d) T. Kohler, T. Biedermann, K. Müller, *Energy Technol.* **2018**, *6*, 1935.

[11] a) G. Whiting, D. Grondin, S. Bennici, A. Auroux, *Sol. Energy Mater. Sol. Cells* **2013**, *112*, 112; b) H. U. Rammelberg, T. Osterland, B. Priehs, O. Opel, W. K. Ruck, *Sol. Energy* **2016**, *136*, 571; c) A. Jabbari-Hichri, S. Bennici, A. Auroux, *Sol. Energy Mater. Sol. Cells* **2017**, *172*, 177; d) K. Posern, C. Kaps, *Thermochim. Acta* **2010**, *502*, 73; e) A. J. Carrillo, D. P. Serrano, P. Pizarro, J. M. Coronado, *J. Mater. Chem. A* **2014**, *2*, 19435.

[12] M. Kubota, S. Matsumoto, H. Matsuda, *Appl. Therm. Eng.* **2019**, *150*, 858.

[13] S. Li, H. Huang, X. Yang, Y. Bai, J. Li, N. Kobayashi, M. Kubota, *Appl. Therm. Eng.* **2018**, *128*, 706.

[14] S. Li, H. Huang, J. Li, N. Kobayashi, Y. Osaka, Z. He, H. Yuan, *RSC Adv.* **2018**, *8*, 8199.

[15] H. Hu, W. Liang, Y. Zhang, S. Wu, Q. Yang, Y. Wang, M. Zhang, Q. Liu, *ACS Sustain. Chem. Eng.* **2018**, *6*, 3830.

[16] a) X. Xu, K. Sielicki, J. Min, J. Li, C. Hao, X. Wen, X. Chen, E. Mijowska, *Renew. Energy* **2022**, *185*, 187; b) J. Min, X. Xu, J. J. Koh, J. Gong, X. Chen, J. Azadmanjiri, F. Zhang, X. Wen, C. He, *ACS Appl. Energy Mater.* **2021**, *4*, 3317; c) J. Li, B. Michalkiewicz, J. Min, C. Ma, X. Chen, J. Gong, E. Mijowska, T. Tang, *Chem. Eng. J.* **2019**, *360*, 250; d) J. Min, X. Xu, J. Li, C. Ma, J. Gong, X. Wen, X. Chen, J. Azadmanjiri, T. Tang, *J. Appl. Polym. Sci.* **2019**, *136*, 48214.

[17] X. Yang, S. Li, H. Huang, J. Li, N. Kobayashi, M. Kubota, *Energies* **2017**, *10*, 644.

[18] H. Yu, H. Dai, Y. Zhu, H. Hu, R. Zhao, B. Wu, D. Chen, *J. Power Sources* **2021**, *481*, 229159.

[19] Y. Fu, N. Zhang, Y. Shen, X. Ge, M. Chen, *Bioresour. Technol.* **2018**, *269*, 67.

[20] W. Zhu, Y. Lin, W. Kang, H. Quan, Y. Zhang, M. Chang, K. Wang, M. Zhang, W. Zhang, Z. Li, H. Wei, T. Fan, D. Chen, H. Hu, *Appl. Surf. Sci.* **2020**, *512*, 145717.

[21] Y. Zhang, L. Deng, H. Hu, Y. Qiao, H. Yuan, D. Chen, M. Chang, H. Wei, *Sustain. Energy Fuels* **2020**, *4*, 1642.

[22] L. Deng, H. Yuan, X. Qian, Q. Lu, L. Wang, H. Hu, Y. Chen, *Resour. Conserv. Recycl.* **2022**, *177*, 105980.

[23] Y. Ma, Y. Li, Y.-P. Zeng, *J. Mater. Sci.* **2021**, *56*, 8588.

[24] H. Hu, Y. Zhang, Y. Qiao, D. Chen, *Appl. Surf. Sci.* **2020**, *508*, 144835.

[25] S. Ghasemi, Z. J. Farsangi, A. Beitollahi, M. Mirkazemi, S. M. Rezayat, S. Sarkar, *Ceram. Int.* **2017**, *43*, 11225.

[26] H. Hu, X. Wang, D. Miao, Y. Wang, C. Lai, Y. Guo, W. Wang, J. H. Xin, H. Hu, *Chem. Commun.* **2015**, *51*, 16699.

[27] H. Hu, J. H. Xin, H. Hu, *J. Mater. Chem. A* **2014**, *2*, 11319.

[28] a) C. Ma, T. Lu, J. Shao, J. Huang, X. Hu, L. Wang, *Sep. Purif. Technol.* **2022**, *281*, 119899; b) S. Liu, L. Rao, P. Yang, X. Wang, L. Wang, R. Ma, L. Yue, X. Hu, *J. Environ. Sci.* **2020**, *93*, 109; c) Z. Zhao, C. Ma, F. Chen, G. Xu, R. Pang, X. Qian, J. Shao, X. Hu, *Biomass Bioenergy* **2021**, *145*, 105969.